Journal of Materials Chemistry A

ROYAL SOCIETY OF CHEMISTRY

COMMUNICATION

View Article Online
View Journal | View Issue

Cite this: J. Mater. Chem. A, 2023, 11, 25262

Received 15th August 2023
Accepted 27th October 2023

DOI: 10.1039/d3ta04899c

rsc.li/materials-a

High throughput identification of complex rutile alloys for the acidic oxygen evolution reaction†

Lan Zhou, [ab] Aniketa Shinde,‡[a] Ming-Chiang Chang, [c] R. Bruce van Dover, [c] Michael O. Thompson[c] and John M. Gregoire [*ab]

Efficient and durable catalysis of the oxygen evolution reaction in acidic media remains a grand challenge at the intersection of electrochemistry and materials discovery. Antimony-based rutile oxides have shown great promise but suffer from poor durability at high concentration of activity-promoting elements such as Mn. We use combinatorial methods to realize a new family of catalysts wherein combinations of Sn, Ti, and Sb enable activity in rutile oxides with Mn concentration less than 40%.

The evolution of O_2 from H_2O (the oxygen evolution reaction, OER, or water oxidation catalysis, WOC) is the most sustainable anodic reaction to liberate protons and electrons that are central to fuel-forming cathodic reactions such as hydrogen evolution (HER), carbon dioxide reduction (CO_2RR), and nitrogen reduction (or fixation, N_2RR).[1,2] Among these, the technology most prepared for widespread deployment readiness is green H_2 production *via* coupling OER and HER in electrolysers. Acidic electrolysers can leverage the deep polymer exchange membrane (PEM) technology and benefit from the favourable HER kinetics in strong acid.[3] The only acid OER catalysts with sufficient activity and durability for commercialization are Ir-based catalysts, for which expense and terrestrial scarcity limit scalability.[2] Pioneering efforts in high throughput discovery of acidic OER catalysts identified optimal precious metal catalyst formulations,[4] and in the present work we deploy these approaches to non-precious metal oxide catalysts in high dimensional composition spaces.

Decades of effort to develop precious-metal-free catalysts[5] yielded few plausible candidates until the recent proliferation of Sb-based oxides, particularly in rutile structures containing first-row transition metals such as Ni, Mn, and Co. In addition to characterizing such catalysts, Mahidashti *et al.* provide an excellent summary of recent progress.[6] Briefly, high throughput experiments from our group revealed that incorporation of Sb, Mn, and Co in an oxide catalyst (Mn–Co–Sb–O) provides an unprecedented combination of activity and stability.[7] A similar combination of elements, Ni–Mn–Sb–O, in a rutile structure was identified,[8] followed by our demonstration of further improving activity *via* transition metal enrichment within the rutile structure (Mn–Sb–O).[9] Computational Pourbaix analysis revealed the thermodynamic basis for the stability of Mn–Sb oxides[9] as well as the broader family of Sb-based rutile oxides under acid OER conditions.[10] The family of catalysts was then expanded to include Co–Sb–O,[11] prompting efforts to optimize properties *via* nanoparticle synthesis of M–Sb–O catalysts with M = Co, Mn, Ni, Fe, and Ru.[12] In an effort to improve the activity of Sb-rich rutile oxides, Luke *et al.*[13] embarked a combinatorial discovery effort based on M–Mn–Sb–O catalysts with M = Ru, Co, Pb, and Cr. Perhaps the most important observation from this work is the improved activity and stability of Mn–Pb–Sb–O catalysts, suggesting that rather than a diversity of transition metals, catalyst optimization may be realized with a diversity of other elements that stabilize Mn active sites.

Collectively, these efforts have demonstrated the stabilization of first row transition metals in Sb-based rutile structures, with a persistent challenge that increasing the Sb concentration increases stability while decreasing OER activity. Despite this challenge, the efforts to develop this family of catalysts continue because they provide the highest activity among non-precious-metal acid OER electrocatalysts with dissolved metals concentrations below 10^{-6} M, a measurement of stability that may serve as a proxy for long-term durability.[14]

For reactions such as acidic OER with non-precious metals, where catalyst stability is a greater challenge than catalyst activity, high throughput experiments are sometimes ineffective due to the limited ability to quickly assess stability. For Sb-based oxides, the systematic trend of increasing stability with decreasing concentration of activity-promoting elements

[a]Division of Engineering and Applied Science, California Institute of Technology, Pasadena, CA, USA. E-mail: gregoire@caltech.edu
[b]Liquid Sunlight Alliance, California Institute of Technology, Pasadena, CA, USA
[c]Department of Materials Science and Engineering, Cornell University, Ithaca, NY, USA

† Electronic supplementary information (ESI) available. See DOI: https://doi.org/10.1039/d3ta04899c

‡ Present address: Nova Measuring Instruments Inc., Portland, OR, USA.

enables the design of a targeted high throughput search for active catalysts with compositions that are desirable with respect to this composition-stability trend. Since the Mn–Sb–O system has already been searched,[9] we drew inspiration from our recent identification of compositionally complex rutile oxides in the Co–Sn–Ta–O system, where both OER activity and electrochemical stability are tuned by composition within the rutile phase.[15]

To design the high throughput campaign, we selected a single activity-promoting element and multiple stability-promoting elements that may collectively form complex rutile-phase electrocatalysts. While historically Co has also been a prevalent element in OER catalyst development, direct comparison of rutile $MnSb_2O_6$ and $CoSb_2O_6$ shows that they have comparable activity.[11] Our study of the phase behaviour in the Mn–Sb–O[9] and Co–Sb–O[16] systems revealed that Mn provides a much broader range of compositions with rutile structure, making Mn our choice for the activity-promoting element. For stability-promoting elements, we considered rutile oxides whose acid stability is well established, leading to the selection of SnO_2 and TiO_2.[17–19] To explore addition of these cation elements individually and collectively we designed compositions libraries in the following composition spaces: Mn–Sn–Sb–O, Mn–Ti–Sb–O, and Mn–Sn–Ti–Sb–O. The Mn–Sb–O from our previous study[9] is a common subsystem that we measured as a baseline alongside the quaternary and quinary oxide systems. We designed combinatorial characterization of these composition space to evaluate a 2-part hypothesis: (1) that complex rutile solid solutions can be formed in these high-order composition spaces, and (2) that integrating Mn with some combination of Sn, Ti, and Sb in a rutile structure will enable higher OER activity at lower Mn concentration than observed in the Mn–Sb–O system.

Each composition library was synthesized *via* reactive co-sputtering from elemental metal targets, as detailed in the ESI.† The orientation of the deposition sources for each continuous composition spread is shown in Fig. 1, where a continuous composition spread within each of the 4 compositions systems was obtained by simultaneously operating the respective deposition sources with thin films collected on a 10 cm-diameter Si wafer with thermal oxide, Ti adhesion layer, and Pt conducting layer. Deposition in an atmosphere of 4.8 mTorr Ar and 1.2 mTorr O_2 followed by annealing in air at 700 °C resulted in metal oxide libraries that were characterized by 3 methods: (i) X-ray fluorescence (XRF) to determine the spatial map of composition, which detects all elements except oxygen and is the source of all composition plots in the present work; (ii) X-ray diffraction (XRD) to characterize the phase behaviour (Fig. 1d); and (iii) scanning droplet cell electrochemistry to characterize OER activity (Fig. 1e).[20]

The phase behaviour of the composition libraries is central to evaluating hypothesis (1). XRD measurements were acquired on 203 samples from the 4 composition libraries, including 8 Mn–Sb–O, 63 Mn–Sn–Sb–O, 66 Mn–Ti–Sb–O, and 66 Mn–Sn–Ti–Sb–O compositions. Using ICDD phases as prototypes, the phase constitution as well as the lattice parameters of each phase were determined *via* a novel XRD analysis tool, CrystalShift.[21] The results are summarized in Fig. 2 and demonstrate fulfilment of hypothesis (1) with 176 phase-pure rutile samples corresponding to formula units of the type $(Mn_{1-x-y-z}Sb_xSn_yTi_z)O_2$ where x can vary from 0.06 to 0.81, y from 0 to 0.33, and z from 0 to 0.38. In each of the 4 composition libraries, the solubility limit of Mn in this type of rutile structure is observed *via* identification of phase fields containing a Mn_2O_3-type phase (see Table S1†). The solubility limits of Sb, Sn, and Ti are not characterized by the present data as no phase boundary beyond phase-pure rutile is observed at compositions enriched in these elements. Given the present goal of studying catalysts with low Mn concentration, the XRD results demonstrate that all compositions with Mn concentration below 0.6

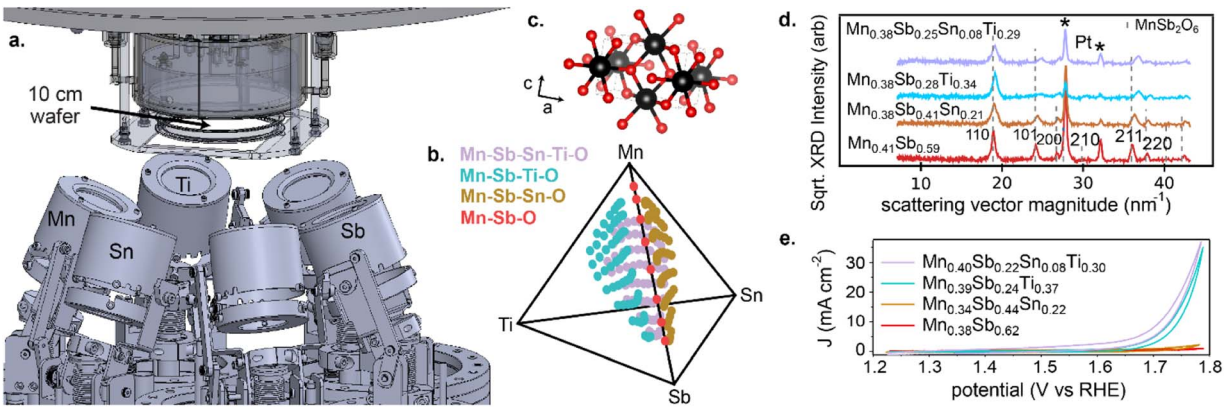

Fig. 1 (a) Illustration of the arrangement of sputter deposition sources for depositing the 4 composition libraries. (b) A composition plot in the Mn–Sb–Sn–Ti–O composition space showing the 182 compositions used in electrochemical experiments, coloured by composition system. (c) An illustration of the rutile crystal structure in which different concentrations of the metal elements are intended to populate the cation sublattice (black), which may also change the vacancy concentration on the oxygen sublattice (red). (d) A representative XRD pattern from each composition space. The 2 peaks from the Pt underlayer are marked, with the remainder of the peaks corresponding to the rutile structure ($MnSb_2O_6$, ICDD entry 04-011-4962). The rutile peaks are labelled by their Miller indices, with deviations from these peak positions among the 4 XRD patterns corresponding to changes in the lattice parameters due to site substitutions within the rutile structure. (e) A representative cyclic voltammogram in 1 M H_2SO_4 from each composition space showing the dramatic influence of Ti incorporation.

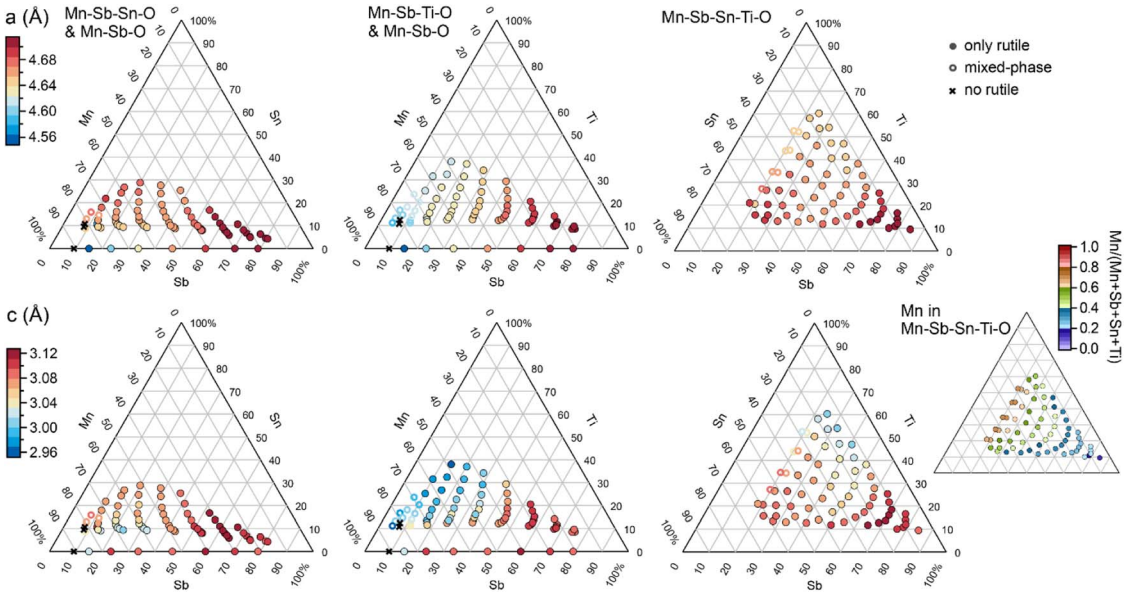

Fig. 2 Summary of the 203 XRD measurements from the 4 composition libraries. Each of the 3 columns of composition plots is labelled with the composition system(s) and contains a top and bottom panel corresponding to the 2 rutile lattice parameters. For the Mn–Sb–Sn–Ti–O system, the Mn concentration is indicated by the smaller, right-most composition plot. Each composition within the 6 lattice parameter plots is plotted as a filled or hollow circle for phase-pure and mixed-phase rutile, respectively, with marker colour indicating the lattice parameter value inferred from the XRD pattern. Only the rutile phase is observed for all compositions with Mn concentration below 0.6. Several Mn-rich samples contain some or no rutile phase. Among the phase-pure rutile samples, both lattice parameters vary systematically with cation composition, indicating a broad range of site substitutions within the rutile structure across each composition space. An alternative composition plot of this data is presented in Fig. S1.†

are amenable to evaluation of hypothesis (2). Electrochemical characterization on 182 samples from the 4 composition libraries included 8 Mn–Sb–O, 62 Mn–Sn–Sb–O, 48 Mn–Ti–Sb–O, and 64 Mn–Sn–Ti–Sb–O compositions. For each composition, electrochemical characterization under continuous flow of 1 M H_2SO_4 electrolyte commenced with a cyclic voltammogram from 1.23 V to 1.79 V *vs.* RHE, and for the present purposes of exploring catalytic activity as a function of cation composition, the geometric current density (using a representative electrolyte contact area of 0.02 cm^2) from the initial cyclic voltammogram experiment at 1.79 V *vs.* RHE is used as the catalytic activity for each composition. This data as well as XRF, XRD, and other electrochemical data are available in an open-source repository.[22]

The OER activity measurements are summarized in Fig. 3 where each composition is shown using its concentration of Mn (with respect to all elements except oxygen). The 8 data points from the Mn–Sb–O library illustrate the aforementioned trend that increased concentration of catalytic elements such as Mn results in increased activity, which must be considered in context of the previous demonstration of decreased durability with increasing Mn concentration.[9] Fig. 3 also illustrates that many compositions from each higher-order composition space exhibit higher activity than the Mn–Sb–O baseline, confirming that integration with multiple stabilizing elements enables higher activity at lower Mn concentration, per hypothesis (2).

To illustrate which additions of Sn and/or Ti improve upon the Mn–Sb–O baseline, Fig. 4 shows the same set of data as Fig. 3 with a series of pseudo-ternary Sb–Sn–Ti compositions plots corresponding to Mn concentration bins: below 0.4, between 0.4 and 0.6, and between 0.6 and 0.8. Graphically, this corresponds to projecting the points within the composition tetrahedron of Fig. 1 to the Sb–Sn–Ti composition triangle,

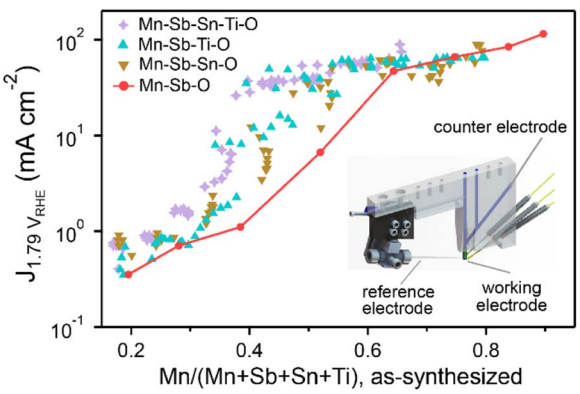

Fig. 3 Summary of the 182 OER activity measurements, each on a unique composition from one of the 4 composition libraries shown in the legend. The OER activity is reported as the current density at 1.79 V *vs.* RHE. The compositions are represented by the metals concentration of Mn. The Mn–Sb–O data points are connected by a line, with any points above this line illustrating an activity improvement at the given Mn concentration *via* incorporation of Sn and/or Ti into the catalyst. The inset contains an illustration of the scanning droplet electrochemical cell used to address each composition and perform electrochemical measurements under in 1 M H_2SO_4.

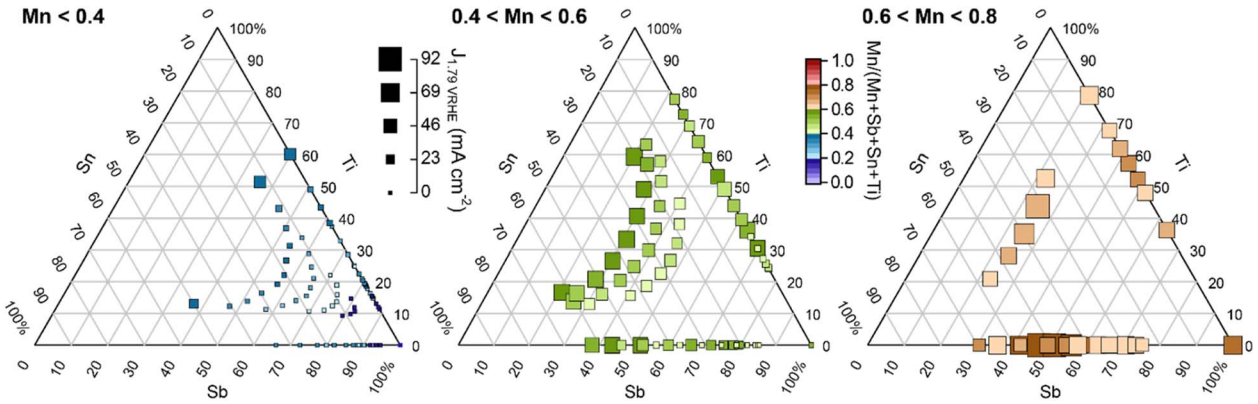

Fig. 4 Summary of 180 OER activity measurements from Fig. 3 with Mn concentrations in the indicated ranges. Within each Mn concentration range, the data are shown using re-normalized Sb–Sn–Ti compositions with the Mn concentration illustrated by the marker colour. The size of each data marker indicates its catalytic activity. The Mn–Sb–O baseline compositions appear at the bottom-right corner of each panel, with any larger points in each graph indicating a benefit of incorporating Sn and/or Ti into the catalyst. Per Fig. 2, only the rutile phase was observed for each composition in the first 2 panels, with the 0.6 < Mn < 0.8 panel containing rutile and mixed-phase samples. An alternative composition plot of this data is presented in Fig. S2.†

which projects all Mn–Sb–O baseline compositions to the 100% Sb corner of each composition triangle. With this plotting scheme, the goal of improving activity through addition of Sn and/or Ti corresponds to achieving higher activity on the Sb–Sn edge, on the Sb–Ti edge, or within the Sb–Sn–Ti region of each composition plot. Fig. 4 shows that this goal is achieved within each of the 3 ranges of Mn concentration (each panel contains points larger than the largest point at the bottom-right corner).

The Mn <0.4 panel of Fig. 4 is most central to the goal of achieving high activity at a composition enriched with elements that typically resist corrosion. Considering only Mn concentrations below 0.4, the highest activity (current density at 1.79 V *vs.* RHE) from the Mn–Sb–O baseline system is 1.1 mA cm^{-2} from the $Mn_{0.38}Sb_{0.62}$ sample. The highest activity from addition of Sn, Ti, and Sn + Ti are as follows: 2.4 mA cm^{-2} from the $Mn_{0.34}Sb_{0.44}Sn_{0.22}$ sample, 35 mA cm^{-2} from the $Mn_{0.39}Sb_{0.24}Ti_{0.37}$ sample, and 37 mA cm^{-2} from the $Mn_{0.40}Sb_{0.22}Sn_{0.08}Ti_{0.30}$ sample, respectively. These correspond to activity improvements at 1.79 V *vs.* RHE by factors of approximately 2, 32, and 34, respectively. The cyclic voltammograms of these exemplar compositions are shown in Fig. 1e.

To further show the realization of activity at low Mn concentration, we can consider samples with Mn concentration below 0.3, which is below that of the quintessential $MnSb_2O_6$ rutile structure that has been central to acid OER studies in this family of catalysts.[8–10] All 9 compositions with low Mn concentration and current density above 1 mA cm^{-2} are found in the quinary oxide space with Sb concentrations between 0.40 and 0.48, Sn concentrations between 0.07 and 0.23, and Ti concentrations between 0.08 and 0.24.

The combinatorial exploration of Mn–Sb–Sn–O, Mn–Sb–Ti–O, and Mn–Sb–Sn–Ti–O composition spaces illustrates that both Sn and Ti can help achieve high activity at low Mn concentration, with Ti providing the best performance enhancement. While the mechanism for improvement must be explored in future work, some lines of inquiry can be established by the present data. An increasingly invoked strategy for catalyst development is to realize a distribution of surface sites, which can be achieved by compositionally complex catalysts,[23] high entropy alloys,[24] or amorphous catalysts.[25] The XRD patterns (Fig. 1d) of the complex rutile electrocatalysts do not reveal any ordering peaks, suggesting that the 3 or 4 cation elements randomly occupy the cation sublattice, which could lead to a surface with a broad distribution of active sites, in particular Mn atoms with different coordination environments. The heterogeneity in the oxidation state of the 3 or 4 cation elements could also lead to the formation of near-surface oxygen vacancies, which have been shown to promote OER activity.[26,27] The importance of Ti incorporation may arise from its compression of the rutile lattice. Compared to rutile $MnSb_2O_6$ with lattice constants of 0.471 and 0.313 nm, rutile SnO_2 has comparable lattice constants, 0.474 and 0.319 nm (ICDD 00-041-1445). Rutile TiO_2 has smaller lattice constants, 0.459 and 0.296 nm (ICDD 00-021-1276). In the composition region of the best low-Mn compositions in the present work, $Mn_{0.39}Sb_{0.24}Ti_{0.37}$ and $Mn_{0.40}Sb_{0.22}Sn_{0.08}Ti_{0.30}$, the rutile lattice constants are approximately 0.465 and 0.3 nm, indicating a compressed lattice compared to the baseline $MnSb_2O_6$, motivating future investigation on the effects of Mn–O and Mn–metal bond distances on the activity of Mn sites for the acidic OER. We also note that the design of the experiments based on improvements to the Mn–Sb–O baseline resulted in biasing exploration of each higher-order composition space to compositions near this baseline, whereas the highest activities are observed with substantial concentrations of Sn and/or Ti, motivating future exploration of compositions with even higher concentrations of these elements.

We show in the ESI the XRD and OER activity characterization of a Mn–Co–Sb–O composition library (Fig. S3†). This library contains a smaller fraction of phase-pure rutile samples due to the formation of $(Mn,Co)_3O_4$ at Co and Mn-rich compositions. Fig. S3† shows that, with respect to the Mn–Sb–

O baseline system, Mn may be substituted by Co and retain appreciable OER activity. However, given that Co is similar to Mn in its propensity for corrosion under acid OER conditions, no compositions in this library substantially outperform the Mn–Sb–O baseline with respect to high OER activity at low concentration of elements prone to corrosion. This observation highlights the opportunities for future catalyst development that build upon our discovery of complex rutile alloys in the Mn–Sb–Sn–Ti–O system (Fig. 2) and their high OER activity at low Mn concentration (Fig. 3 and 4).

Conclusions

The electrocatalysis community has had an awakening regarding the fundamental science challenges that underlie operational durability, which is particularly important in non-precious-metal acid OER catalysis.[28] The measurement of equilibrated dissolved metals concentration may serve as an important indicator of long-term durability,[14] and while there have been initial demonstrations of time-resolved measurements *via* online detection,[29,30] such measurements remain prohibitively expensive for high throughput exploration of high dimensional composition spaces. The present work focuses on decreasing the concentration of elements most prone to corrosion by exploring quaternary and quinary oxides in which Mn is mixed with various combinations of Sb, Sn, and Ti. XRD analysis confirms that a site-substituted rutile phase can be synthesized over a broad range of compositions in the Mn–Sb–Sn–Ti–O composition space. The results demonstrate a catalyst motif wherein activity is realized at low concentration of the presumed catalytic element (Mn) *via* integration with multiple elements that resist corrosion (Sn, Ti, Sb). The incorporation of Ti is particularly impactful, which may be related to its compression of the rutile structure.

Data availability

In addition to summary tables in the ESI, all raw and analysed data are available at **https://data.caltech.edu/doi/10.22002/tg041-j4g80** (doi: **10.22002/tg041-j4g80**).

Author contributions

L. Z. synthesized all catalysts, performed materials characterization experiments, aggregated all data, and developed data visualization schemes that produced the primary data figures. A. S. performed electrochemical experiments. M. C. performed CrystalShift XRD analysis under supervisions of M. O. T. and R. B. vD. J. M. G. designed the experimental campaign, supervised research, and was the primary author of the communication with contributions from all authors.

Conflicts of interest

J. M. G. is a consultant for companies that aim to accelerate catalyst discovery.

Acknowledgements

This material is primarily based on work performed by the Liquid Sunlight Alliance, which is supported by the U.S. Department of Energy, Office of Science, Office of Basic Energy Sciences, Fuels from Sunlight Hub under Award DE-SC0021266. Data acquisition was also supported by the Joint Center for Artificial Photosynthesis, a DOE Energy Innovation Hub, supported through the Office of Science of the U.S. Department of Energy (Award No. DE-SC0004993). X-ray diffraction analysis was performed by the Scientific Autonomous Reasoning Agent (SARA), supported by the Air Force Office of Scientific Research under award FA9550-18-1-0136. The authors thank Yungchieh Lai and Dan Guevarra for assistance with data analysis, and Ryan J. R. Jones and Kevin Kan for assistance with experiments.

Notes and references

1 V. Charles, A. O. Anumah, K. A. Adegoke, M. O. Adesina, I. P. Ebuka, N. A. Gaya, S. Ogwuche and M. O. Yakubu, *Sustainable Mater. Technol.*, 2021, **28**, e00252.
2 C. C. L. McCrory, S. Jung, I. M. Ferrer, S. M. Chatman, J. C. Peters and T. F. Jaramillo, *J. Am. Chem. Soc.*, 2015, **137**, 4347–4357.
3 Z. Chen, L. Guo, L. Pan, T. Yan, Z. He, Y. Li, C. Shi, Z.-F. Huang, X. Zhang and J.-J. Zou, *Adv. Energy Mater.*, 2022, **12**, 2103670.
4 D. Seley, K. Ayers and B. a Parkinson, *ACS Comb. Sci.*, 2013, **15**, 82–89.
5 S. Cherevko, *Curr. Opin. Electrochem.*, 2023, **38**, 101213.
6 Z. Mahidashti, M. Rezaei, M. Borrelli and A. Shaygan Nia, *J. Electroanal. Chem.*, 2023, **937**, 117404.
7 A. Shinde, R. J. R. Jones, D. Guevarra, S. Mitrovic, N. Becerra-Stasiewicz, J. A. Haber, J. Jin and J. M. Gregoire, *Electrocatalysis*, 2015, **6**, 229–236.
8 I. A. Moreno-Hernandez, C. A. MacFarland, C. G. Read, K. M. Papadantonakis, B. S. Brunschwig and N. S. Lewis, *Energy Environ. Sci.*, 2017, **10**, 2103–2108.
9 L. Zhou, A. Shinde, J. H. Montoya, A. Singh, S. Gul, J. Yano, Y. Ye, E. J. Crumlin, M. H. Richter, J. K. Cooper, H. S. Stein, J. A. Haber, K. A. Persson and J. M. Gregoire, *ACS Catal.*, 2018, **8**, 10938–10948.
10 G. T. K. K. Gunasooriya and J. K. Nørskov, *ACS Energy Lett.*, 2020, **5**, 3778–3787.
11 T. A. Evans and K.-S. Choi, *ACS Appl. Energy Mater.*, 2020, **3**, 5563–5571.
12 S. Luke, M. Chatti, A. Yadav, B. V. Kerr, J. Kangsabanik, T. Williams, P. V. Cherepanov, B. Johannessen, A. Tanksale, D. R. MacFarlane, R. K. Hocking, A. Alam, A. Yella and A. N. Simonov, *J. Mater. Chem. A*, 2021, **9**, 27468–27484.
13 S. Luke, M. Chatti, D. Simondson, K. N. Dinh, B. V. Kerr, T. D. Nguyen, G. Yilmaz, B. Johannessen, D. R. MacFarlane, A. Yella, R. K. Hocking and A. N. Simonov, *EES Catal.*, 2023, **1**, 730–741.
14 K. K. Rao, Y. Lai, L. Zhou, J. A. Haber, M. Bajdich and J. M. Gregoire, *Chem. Mater.*, 2022, **34**, 899–910.

15 L. Yang, J. A. Haber, Z. Armstrong, S. J. Yang, K. Kan, L. Zhou, M. H. Richter, C. Roat, N. Wagner, M. Coram, M. Berndl, P. Riley and J. M. Gregoire, *Proc. Natl. Acad. Sci. U. S. A.*, 2021, **118**(37), e2106042118.
16 L. Zhou, H. Li, Y. Lai, M. Richter, K. Kan, J. A. Haber, S. Kelly, Z. Wang, Y. Lu, R. S. Kim, X. Li, J. Yano, J. K. Nørskov and J. M. Gregoire, *ACS Energy Lett.*, 2022, 993–1000.
17 M. Wu, Y. Li, J. Du, C. Tao and Z. Liu, *Appl. Surf. Sci.*, 2019, **495**, 143596.
18 F. Wu, Z.-Q. Yang, W. Sun, X. Chen, H. Qi and L.-D. Wang, *Ind. Eng. Chem. Res.*, 2022, **61**, 12349–12358.
19 J. Tong, Y. Liu, Q. Peng, W. Hu and Q. Wu, *J. Mater. Sci.*, 2017, **52**, 13427–13443.
20 J. M. Gregoire, C. Xiang, X. Liu, M. Marcin and J. Jin, *Rev. Sci. Instrum.*, 2013, **84**, 024102.
21 M. C. Chang, S. Ament, M. Amsler, D. R. Sutherland, L. Zhou, J. M. Gregoire, C. P. Gomes, R. B. van Dover and M. O. Thompson, Probabilistic Phase Labeling and Lattice Refinement for Autonomous Material Research, *arxiv*, 2023, preprint, arXiv:2308.07897 [cond-mat.mtrl-sci], DOI: **10.48550/arXiv.2308.07897**.
22 L. Zhou and J. M. Gregoire, High throughput oxygen evolution reaction data for oxide catalysts containing Mn, Sb, Sn, Ti, and Co, *CaltechData*, 2023, DOI: **10.22002/tg041-j4g80**.
23 Y. Yao, Z. Huang, T. Li, H. Wang, Y. Liu, H. S. Stein, Y. Mao, J. Gao, M. Jiao, Q. Dong, J. Dai, P. Xie, H. Xie, S. D. Lacey, I. Takeuchi, J. M. Gregoire, R. Jiang, C. Wang, A. D. Taylor, R. Shahbazian-Yassar and L. Hu, *Proc. Natl. Acad. Sci. U. S. A.*, 2020, **117**, 6316–6322.
24 J. You, R. Yao, W. Ji, Y. Zhao and Z. Wang, *J. Alloys Compd.*, 2022, **908**, 164669.
25 T. Guo, L. Li and Z. Wang, *Adv. Energy Mater.*, 2022, **12**, 2200827.
26 J. M. Spurgeon, J. M. Velazquez and M. T. McDowell, *Phys. Chem. Chem. Phys.*, 2014, **16**, 3623–3631.
27 S. Kumari, B. P. Ajayi, B. Kumar, J. B. Jasinski, M. K. Sunkara and J. M. Spurgeon, *Energy Environ. Sci.*, 2017, **10**, 2432–2440.
28 M. Risch, *Curr. Opin. Electrochem.*, 2023, **38**, 101247.
29 S. Cherevko and K. J. J. Mayrhofer, in *Encyclopedia of Interfacial Chemistry*, ed. K. Wandelt, Elsevier, Oxford, 2018, pp. 326–335.
30 K. J. Jenewein, S. Thienhaus, A. Kormányos, A. Ludwig and S. Cherevko, *Chem. Sci.*, 2022, **13**, 13774–13781.